J|A|C|S
ARTICLES
Published on Web 03/15/2007

Core/Shell Quantum Dots with High Relaxivity and Photoluminescence for Multimodality Imaging

Shizhong Wang,[†,‡] Benjamin R. Jarrett,[‡] Susan M. Kauzlarich,[†] and Angelique Y. Louie*,[‡]

Contribution from the Department of Chemistry, and Department of Biomedical Engineering, University of California, Davis, California 95616

Received August 17, 2006; E-mail: aylouie@ucdavis.edu

Abstract: A series of core/shell CdSe/$Zn_{1-x}Mn_xS$ nanoparticles were synthesized for use in dual-mode optical and magnetic resonance (MR) imaging techniques. Mn^{2+} content was in the range of 0.6−6.2% and varies with the thickness of the shell or amount of Mn^{2+} introduced to the reaction. These materials showed high quantum yield (QY), reaching 60% in organic solvent. Water-soluble nanoparticles were obtained by capping the core/shell particles with amphiphilic polymer, and the QY values in water reached 21%. These materials also demonstrated high relaxivity with r_1 values in the range of 11−18 mM^{-1} s^{-1} (at room temperature, 7 T). Both optical and MR imaging were performed on nanoparticles in aqueous solution and applied to cells in culture. The results showed that the QY and manganese concentration in the particles was sufficient to produce contrast for both modalities at relatively low concentrations of nanoparticles.

Introduction

The recognition that many biomedical imaging modalities provide complementary information has stimulated intense interest in multimodality imaging, using more than one modality to probe a sample of interest. Commercial dual-modality instruments, such as PET/CT, already have found their way into the clinic.[1,2] The marriage of magnetic resonance imaging and optical techniques represents another complementary imaging pair with potential clinical utility. MRI offers the ability to follow the distribution of molecules in vivo or provide anatomical reference, while optical techniques can be applied to obtain detailed information at subcellular levels.[3,4] Parallel with the growth in multimodal methods has been increased attention to developing multimodality imaging probes. To optimize the use of multiple modalities and to register images from each, ideally a single probe detectable by multiple modalities would be employed. For example, MRI/optical probes have been designed that involve attachment of organic dyes to iron oxide nanoparticles[5−7] or attachment of Gd chelates to quantum dots[8] or to fluorescently tagged polymers.[9] While multimodal probes can be made by simply conjugating probes of different functionality, a more elegant solution is to incorporate multiple functionalities in a single probe. Bifunctional core/shell quantum dots have been described; however, combined high relaxivity for MRI and high quantum yield luminescence have not been reported for these materials.[10−13]

Semiconductor nanoparticles have been exploited as optical indicators because of their narrow, tunable, symmetric emission spectrum.[3,14,15] The benefits of being able to excite with a broad excitation energy and obtain multicolored luminescence has been one of the advantages of semiconductor nanoparticles. In addition, emission is environmentally stable as the production of photons stems from a band gap process rather than the singlet−singlet transition typical for small molecule fluorophores. Recently, there has been considerable interest in Mn^{2+}-doped II−VI nanoparticles[16−18] for technological applications such as spin injectors and magnetic memory elements.[19] However, it is difficult to directly dope Mn^{2+} into CdSe, an

[†] Department of Chemistry.
[‡] Department of Biomedical Engineering.

(1) Wechalekar, K.; Sharma, B.; Cook, G. *Clin. Radiol.* **2005**, *60*, 1143−55.
(2) Antoch, G.; Vogt, F. M.; Freudenberg, L. S.; Nazaradeh, F.; Goehde, S.; Barkhausen, J.; Dahmen, G.; Bockisch, A.; Debatin, J. F.; Ruehm, S. G. *JAMA, J. Am. Med. Assoc.* **2003**, *290*, 3199−3206.
(3) Alivisatos, P. *Nat. Biotechnol.* **2004**, *22*, 47−52.
(4) Cherry, S. *Phys. Med. Biol.* **2004**, *49*, R13−R48.
(5) Tsourkas, A.; Shinde-Patil, V. R.; Kelly, K. A.; Patel, P.; Wolley, A.; Allport, J. R.; Weissleder, R. *Bioconjugate Chem.* **2005**, *16*, 576−581.
(6) Lu, Y.; Yin, Y.; Mayers, B. T.; Xia, Y. *Nano Lett.* **2002**, *2*, 183−186.
(7) Huh, Y. M.; Jun, Y. W.; Song, H. T.; Kim, S.; Choi, J. S.; Lee, J. H.; Yoon, S.; Kim, K. S.; Shin, J. S.; Suh, J. S.; Cheon, J. *J. Am. Chem. Soc.* **2005**, *127*, 12387−12391.
(8) Mulder, W.; Koole, R.; Brandwijk, R.; Storm, G.; Chin, P. T. K.; Strijkers, G.; deMelloDonega, C.; Nicolay, K.; Griffioen, A. *Nano Lett.* **2006**, *6*, 1−6.
(9) Hueber, M.; Staubli, A.; Kustedjo, K.; Gray, M.; Shih, J.; Fraser, S.; Jacobs, R.; Meade, T. *Bioconjugate Chem.* **1998**, *9*, 242−249.
(10) Green, M. *Small* **2005**, *1*, 684−686.
(11) Kim, H.; Achermann, M.; Balet, L. P.; Hollingsworth, J. A.; Klimov, V. I. *J. Am. Chem. Soc.* **2005**, *127*, 544−546.
(12) Santra, S.; Yang, H.; Holloway, P. H.; Stanley, J. T.; Mericle, R. A. *J. Am. Chem. Soc.* **2005**, *127*, 1656−7.
(13) Wang, G.-P.; Song, E.-Q.; Xie, H.-Y.; Zhang, Z.-L.; Tian, Z.-Q.; Zuo, C.; Pang, D.-W.; Wu, D.-C.; Shi, Y.-B. *Chem. Commun.* **2005**, 4276−4278.
(14) Empedocles, S. A.; Neuhauser, R.; Shimizu, K.; Bawendi, M. G. *Adv. Mater.* **1999**, *11*, 1243−1256.
(15) Gao, X.; Cui, Y.; Levenson, R. M.; Chung, L. W. K.; Nie, S. *Nat. Biotechnol.* **2004**, *22*, 969−976.
(16) Azad Malik, M.; O'Brien, P.; Revaprasadu, N. *J. Mater. Chem.* **2001**, *11*, 2382−2386.
(17) Norman, T. J.; Magana, D.; Wilson, T.; Burns, C.; Zhang, J. Z.; Cao, D.; Bridges, F. *J. Phys. Chem. B* **2003**, *107*, 6309−6317.
(18) Zu, L.; Norris, D. J.; Kennedy, T. A.; Erwin, S. C.; Efros, A. L. *Nano Lett.* **2006**, *6*, 334−340.

10.1021/ja065996d CCC: $37.00

extremely high luminescence material. To date, there have been only a few successful strategies reported for directly doping Mn^{2+} into CdSe nanoparticles: incorporation of Mn^{2+} into wurtzite CdSe via the use of a prebonded complex as the precursor,[20-22] and controlling the growth of zinc blende structure of CdSe with subsequent doping of Mn^{2+}.[23] However, only low levels of Mn^{2+} were incorporated, and doping directly with a transition metal element affected the optical properties: dopants typically quench luminescence.[17,24,25]

In this work, we describe a method to maintain strong photoemission while introducing paramagnetism by capping luminescent nanoparticle cores with a paramagnetically doped ZnS surface. The layered quantum dot design with a paramagnetic ion doped into the shell avoids the use of environmentally sensitive organic dyes and capitalizes on the exquisite stability of quantum dot emission to degradation, environment, or bleaching. This idea is applicable to all of the various core/shell-type structures composed of II−VI-based quantum dots.[26] Further functionalization can be achieved by attaching targeting moieties to these nanoparticles through free amines at the surface to label specific molecular events in disease. For example, with tumor-targeted agents, MRI could be employed to localize lesions. During subsequent surgical resection, optical methods could guide identification of tumor borders. Such multimodal methods hold great promise for improving diagnosis and therapy of diseased states.

We have prepared CdSe cores of various sizes with $Zn_{1-x}Mn_xS$ shells from approximately 1−6 monolayers in thickness. Our synthetic method is a stepwise synthesis with the surface termination separate from nanoparticle growth, providing control over surface doping. Photoluminescence of the CdSe/$Zn_{1-x}Mn_xS$ nanoparticles was studied as a function of size. In addition, for the same core size, we have varied the amount of Mn^{2+} that can be doped into the shell. Thicker shells were prepared of approximately 6 monolayers to confirm incorporation of the Mn^{2+} into the shell, and the effect of Mn^{2+} in thin and thick shells on relaxivity for MRI applications was determined. The resulting nanoparticles have been characterized with X-ray powder diffraction (XRD), transmission electron microscopy (TEM), atomic absorption (AA), electron paramagnetic resonance (EPR), and optical absorbance and photoluminescence (PL). Magnetic resonance measurements and confocal imaging along with cell uptake studies are included to demonstrate that these nanoparticles will be useful for dual-mode magnetic resonance and optical imaging. These CdSe/$Zn_{1-x}Mn_xS$ nanoparticles are a model system for dual modality probes, but these methods may be extended to other inorganic core/shell nanoparticle compositions.

Experimental Section

Chemicals. Chemicals were used as received, unless stated otherwise. Trioctylphosphine oxide (TOPO, tech. 90%), trioctylphosphine (TOP, tech. 90%), hexadecylamine (HDA, tech. 90%), cadmium acetate (98%), manganese chloride (99.99%), manganese acetate tetrahydrate (99.99%), diethylzinc (1.0 M solution in hexane), methylmagnesium chloride (3.0 M solution in tetrahydrofuran), poly(acrylic acid, sodium salt (average $M_w \approx 8000$), 45% solution in water), and octylamine (99%) were obtained from Aldrich. *N*-(3-Dimethylaminopropy)-*N*′-ethyl-carbodiimide (EDC, >97%) was obtained from Fluka. H_2S gas was obtained from Fisher. TOPO and HDA were dried and degassed in the reaction vessel by heating under vacuum for 1 h at about 180 and 140 °C, respectively.

Synthesis of CdSe Core. CdSe nanoparticles were synthesized with slight modifications based on a reported procedure.[27] Briefly, in a 250 mL flask, 8 g of TOPO and 5 g of HDA were added and dried and degassed in vacuo at high temperature. This mixture was allowed to cool under flowing argon to about 120 °C, and a stock solution of 0.139 g of Se dissolved in 3 mL of TOP was added. The temperature was then raised to 300 °C, and another stock solution of 0.12 g of cadmium acetate dissolved in 2 mL of TOP was quickly injected under rapid stirring, under flowing argon. The temperature was then decreased to 260 °C for the crystal growth of CdSe particles for a specific length of time depending on the particle size. The product of CdSe nanoparticles was then isolated with the solvent pair, chloroform and methanol.

Synthesis of Core/Shell CdSe/$Zn_{1-x}Mn_xS$ Nanoparticles. Approximately 1.5 or 6 monolayers of $Zn_{1-x}Mn_xS$ shell were grown on the CdSe core via a postsynthesis method. The amount of Zn and Mn precursor needed to grow a shell of desired thickness was determined from the ratio between the core and shell volumes using bulk lattice parameters of CdSe and ZnS. The definition of one ZnS monolayer is a shell that measures 3.1 Å (the distance between consecutive planes along the [002] axis in bulk wurtzite ZnS). A solution containing 8 g of TOPO and 5 g of HDA was dried and degassed in vacuo at high temperature, and then the temperature was dropped to 100 °C. To this solution was added 0.25 mmol (for ∼1.5 monolayer shell) or 0.1 mmol (for ∼6 monolayer shell) of CdSe nanoparticles dispersed in chloroform, and the chloroform was removed in vacuo. The temperature of the solution was then raised to 170 °C. Stoichiometric amounts of diethylzinc and dimethylmanganese (freshly prepared via a method described in Taumra et al.[28]) were dissolved in 2 mL of TOP. This solution was then injected in 5 portions with intervals of 10 min into the TOPO, HDA solution containing the CdSe nanoparticles. H_2S gas was simultaneously injected into the flask in aliquots of 1 mL at intervals of 5 min. The amount of H_2S was controlled at 4 mL for each of 0.1 mmol of diethylzinc and dimethylmanganese. The reaction temperature was kept at 170 °C for 2 h.

Surface Modification and Water-Soluble QDs. Water-soluble QDs were prepared by capping the QDs with an amphiphilic polymer of octylamine-modified poly(acrylic acid).[29] This procedure was as follows: 10 g of poly(acrylic acid, sodium salt) was diluted 2-fold in water and acidified with 15 mL of 12 N hydrochloride acid. This solution was then dialyzed in water for ∼48 h to remove sodium chloride and the excess of hydrochloride acid. The solution was then heated to approximately 60 °C under vacuum to remove the water. After being fully dried, 72 mg of the polymer was dissolved in 30 mL of dimethylformamide (DMF) and reacted with 75 μL of *n*-octylamine, using 100 μL of ethyl-3-dimethyl amino propyl carbodiimide (EDC) as a cross-linking reagent (45% of carboxyl groups in the polymer were modified). The reaction system was placed under an Ar atmosphere and stirred overnight. Solvent was then removed by vacuum, and the resulting oily product was precipitated with 2 mL of 2 N hydrochloride acid and was rinsed with water five times to remove excess EDC and other byproducts. After vacuum drying, 20 mg of the product was then dissolved in 10 mL of chloroform. To this polymer solution was added

(19) Wolf, S. A.; Awschalom, D. D.; Buhrman, R. A.; Daughton, J. M.; von Molnar, S.; Roukes, M. L.; Chtchelkanova, A. Y.; Treger, D. M. *Science* **2001**, *294*, 1488−1495.
(20) Mikulec, F. V.; Kuno, M.; Bennati, M.; Hall, D. A.; Griffin, R. G.; Bawendi, M. G. *J. Am. Chem. Soc.* **2000**, *122*, 2532−2540.
(21) Jian, W. B.; Fang, J.; Ji, T.; He, J. *Appl. Phys. Lett.* **2003**, *83*, 3377−3379.
(22) Magana, D.; Perera, S. C.; Harter, A. G.; Dalal, N. S.; Strouse, G. F. *J. Am. Chem. Soc.* **2006**, *128*, 2931−2939.
(23) Erwin, S. C.; Zu, L.; Haftel, M. I.; Efros, A. L.; Kennedy, T. A.; Norris, D. J. *Nature* **2005**, *436*, 91−94.
(24) Biswas, S.; Kar, S.; Chaudhuri, S. *J. Phys. Chem. B* **2005**, *109*, 17526−17530.
(25) Bol, A. A.; Meijerink, A. *J. Phys. Chem. B* **2001**, *105*, 10197−10202.
(26) Medintz, I. L.; Uyeda, H. T.; Goldman, E. R.; Mattoussi, H. *Nat. Mater.* **2005**, *4*, 435−446.
(27) Mekis, I.; Talapin, D. V.; Kornowski, A.; Haase, M.; Weller, H. *J. Phys. Chem. B* **2003**, *107*, 7454−7462.
(28) Tamura, M.; Kochi, J. *J. Organomet. Chem.* **1971**, *29*, 111−29.
(29) Wang, K. T.; Iliopoulos, I.; Audebert, R. *Polym. Bull.* **1988**, *20*, 577−82.

10 mL of 5 μmol of isolated QDs in 10 mL of chloroform. The solvent was pumped off under vacuum. The polymer-capped QDs were readily dissolved in 4 mL of water, and then centrifuged in a dialysis tube to remove the excess of polymer.

Characterization. XRD, TEM. XRD patterns were recorded by a Scintag PAD-V X-ray powder diffractometer using Cu K_α radiation (λ = 1.5418 Å) and plotted with Material Data Inc. (MDI) JADE6 software. The XRD patterns were collected between 20° < 2θ < 60° with a dwell time of 2 s and a step size of 0.02 (2θ). For TEM, the nanoparticles were imaged using a Phillips CM-120 transmission electron microscope at an accelerating voltage of 80 kV with sample solution dropped on holey and continuous carbon-coated 400 mesh copper grid.

UV−Vis, PL. UV−vis and PL spectra were obtained on a Cary 100 Bio spectrometer (Varian) and FluoroMax-3P fluorometer, respectively. Quantum yield (QY) was obtained by comparison of the PL intensity of a solution of the nanocrystal sample with that of a solution of Rhodamine 6G (R6G) (laser grade) in ethanol.[30] Isolated QDs were dissolved in chloroform and measured in a standard 1-cm quartz cell with controlled optical densities below 0.10 at the excitation wavelength.

AA. Elemental analysis was carried out on an atomic absorption (AA) spectrophotometer Varian AA 220FS using an air/acetylene flame. The read delay chosen was 6.0 s, and the optical wavelength used was 279.5, 213.9, and 228.8 nm for Mn, Zn, and Cd, respectively. The nanoparticle preparations were assessed after four separations/purifications with the solvent pair of chloroform/methanol. To remove the free manganese absorbed on the surface of CdSe/$Zn_{1-x}Mn_xS$, surface ligand exchange with pyridine was then performed by using published methods.[31] Briefly, the quantum dots were first isolated and then washed four times with chloroform/methanol, and then the precipitated quantum dots were dissolved in pyridine, and the system was stirred overnight. Next, the sample was centrifuged to remove the trace amount of precipitate that sometimes formed. The quantum dots in pyridine were then precipitated by adding hexane followed by centrifugation. This step was repeated, and precipitated quantum dots were dissolved in pyridine again and stirred for 5−6 additional hours, and again precipitated with hexane. Nanoparticle concentration was estimated on the basis of the measured Cd^{2+} concentration and the predicted number of Cd^{2+} ions for a particular nanoparticle diameter. Specifically, the nanoparticle core diameter was determined from the optical properties (absorption spectra),[32] and the number of Cd^{2+} ions per particle was estimated on the basis of the crystal structure and volume of the nanoparticle. The measured Cd^{2+} concentration was then divided by the estimated number of Cd^{2+} ions per particle to obtain a nanoparticle concentration. The purified samples were also used for EPR and relaxivity measurements (see below).

EPR. Continuous wave EPR was taken on a Bruker ECS106 X-Band spectrometer, equipped with an Oxford Instruments liquid helium cryostat. Typical experimental conditions were frequency 9.68 GHz, temperature 4.2 K, modulation amplitude 10 G, microwave power 0.50 m, conversion time 40.96 ms, time constant 40.96 ms, resolution 2048 pts, average of 6 scans.

Magnetic Resonance Imaging (MRI). Characterization of magnetic resonance properties of the manganese-doped particles was achieved by NMR relaxivity. MRI imaging experiments were performed at room temperature on a Biospec 7 T system (Bruker, Billerica, MA) equipped with the standard gradient set, 95 mT/m maximum gradient, and 72 mm inner diameter (i.d.) volume coil. The longitudinal (r_1) relaxivity was determined as the slope of the line for plots of $1/T_1$, against increasing manganese concentration with a correlation coefficient greater than 0.95. T_1 was measured using a sequence of spin echo images with independently varying recovery times (10 data points, TR, 400−5000 ms).[33] T_1-weighted (T1W) images were acquired during the T_1 measurements at a specific TR. Imaging parameters for T1W images were FOV = 4.5 cm, slice thickness 1.2 mm, TR = 800 ms, TE = 10 ms.

Quantum Dot Uptake by P388D1 Cells (Mouse Macrophages). P388D1 cells were plated at 500,000 cells/mL (1 mL per well, 35 mm diameter or 2 mL per well, 70 mm diameter), allowed to adhere to the dish (24 h), and then the media was replaced with lipoprotein-deficient serum (LPDS), RPMI, and cultured for 20 h at 37 °C in a 5% CO_2 atmosphere. Before use on cells, quantum dots were ultrafiltered (Amicon 8010, 100,000 MWCO filter) against 1X PBS (15 mL) to wash away any excess reagents and exchange the buffer for cell studies. After activation, adherent cells were washed three times with 1X PBS, and quantum dots (10% initial Mn, 6 monolayer at 0.0408 mM Mn) in LPDS-RPMI were applied to the cells. The cells were incubated with the particles for 1 h at 37 °C in 5% CO_2 atmosphere. Cells were incubated with quantum dots in separate dishes in parallel for confocal and relaxometry/MRI experiments so that the loss of cells during confocal imaging would not affect relaxometry/MRI data. Cells were then washed three times with 1X PBS, and then 1 mL of CO_2 independent media was added for confocal imaging or for the MR samples, 1 mL of nanopure water was added, and the freeze−thaw method was repeated three times to lyse cells. Cell lysate from two dishes was put into 1.5 mL conical tubes, concentrated by drying (speed vacuum) to 0.25 mL, combined, and used for relaxometry and later MRI.

Confocal Microscopy. Cells were imaged with a Zeiss LSM 5 Pascal confocal microscope equipped with a LD-neofluar 40×/0.6 corr objective. An excitation wavelength of 488 nm (25% power) was used with a 488 nm HFT beam splitter, and a 505 nm low pass filter. A 1024 × 1024 matrix (230.3 × 230.3 μm^2 in-plane resolution), pinhole of 1 Airy unit, and a scan speed of 2 (56.2 μs pixel time) were used. For the 3D acquisition, a 1024 × 1024 × 9 matrix was used with a scan speed of 3 (25.6 pixel time) for a total scan time of approximately 10 min.

Relaxometry. Cells lysate from control cells and cells incubated with quantum dots were put into glass tubes. Approximately 2 million cells were put into each tube for relaxometry for each cell type. T_1 values of control cells (no quantum dots) and cells incubated with quantum dots were determined at 60 MHz and 37 °C using a Bruker Minispec mq60 using an inversion recovery sequence (12 data points).

Magnetic Resonance Imaging. Cell lysates (used for relaxometry) were imaged at 7 T, 21 °C (Bruker Biospec, Billerica, MA) using the standard gradient set (95 mT/m maximum gradient) and 72 mm ID volume coil. A T1W FLASH sequence was used with a FOV = 4 × 4 cm^2, a 128 × 128 matrix, and slice thickness of 0.8 mm. Other scan parameters were TR = 200 ms, TE = 3.05 ms, a flip angle of 60° number of acquisitions = 4, and an echo position of 35%.

Results and Discussion

Scheme 1 outlines the method for preparing the nanoparticles and making them water-soluble. The synthesis described was designed to produce a shell with ~1.5 monolayers of ZnS to maximize luminescence by fully coating CdSe and providing the Mn^{2+} ions at the surface of the nanoparticles to maximize the paramagnetic effect on the relaxivity of surrounding water molecules. Thick shells with approximately 6 monolayers of ZnS were also prepared via this method to confirm the effect of Mn^{2+}. The surface of the synthesized core/shell CdSe/$Zn_{1-x}Mn_xS$ nanoparticles was coated with hydrophobic ligands of

(30) Donega, C. D.; Hickey, S. G.; Wuister, S. F.; Vanmaekelbergh, D.; Meijerink, A. *J. Phys. Chem. B* **2003**, *107*, 489−496.
(31) Kuno, M.; Lee, J. K.; Dabbousi, B. O.; Mikulec, F. V.; Bawendi, M. G. *J. Chem. Phys.* **1997**, *106*, 9869−9882.
(32) Murray, C. B.; Norris, D. J.; Bawendi, M. G. *J. Am. Chem. Soc.* **1993**, *115*, 8706−8715.
(33) Perrin Rosalind, L.; Ivancevic Marko, K.; Kozerke, S.; Vallee, J.-P. *J. Magn. Reson. Imaging* **2004**, *20*, 1030−8.

Scheme 1. Synthetic Route for Generation of Water-Soluble Core/Shell CdSe/$Zn_{1-x}Mn_xS$

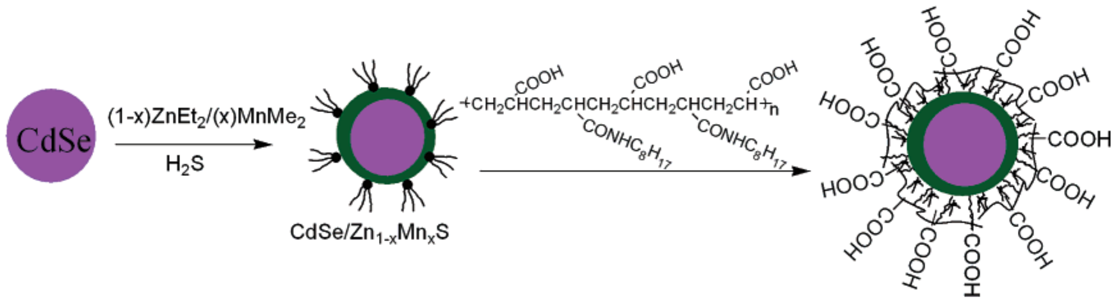

TOPO and HDA, which have a strong interaction with the hydrophobic moiety of the amphiphilic polymer. Figure 1 shows the XRD patterns of CdSe (black) and core/shell CdSe/Zn_{1-x}-Mn_xS (red) nanoparticles along with the expected diffraction peaks for bulk CdSe (wurtzite structure) indicated by vertical lines providing the position (2θ) and relative intensity. The diffraction pattern was obtained before the nanoparticles were made water-soluble. All of the diffraction peaks of the CdSe core can be indexed as the wurtzite structure of CdSe. The large peak at 20−30° (2θ) is consistent with the production of small nanoparticles in which the three low angle peaks tend to overlap and emerge as a single peak. The core/shell CdSe/$Zn_{1-x}Mn_xS$ possessed the same diffraction pattern but was very slightly shifted toward higher 2θ range. The small shift to higher 2θ is characteristic of the formation of core/shell CdSe/ZnS nanoparticles[34] and provides evidence that the CdSe/$Zn_{1-x}Mn_xS$ nanoparticles described herein are core/shell nanoparticles. No additional peaks corresponding to ZnS or MnS were observed, and there is no systematic shifting of all peaks that might indicate formation of a $Cd_{1-x}Zn_xSe$ alloy. Diameters of the nanoparticles were measured by TEM before and after capping.

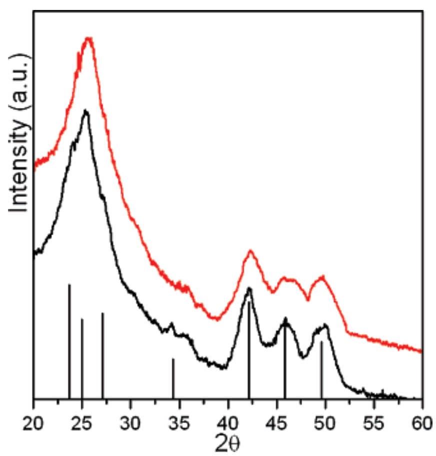

Figure 1. XRD patterns of CdSe (black) and core/shell CdSe/$Zn_{1-x}Mn_xS$ (red) nanoparticles reveal that the CdSe nanoparticle core is the wurtzite structure and the structure is maintained after the growth of the $Zn_{1-x}Mn_xS$ shell. The vertical lines indicate the intensities and position of the expected diffraction pattern for the wurtzite structure of bulk CdSe (from left to right 2θ (*hkl*): 23.70 (100), 25.01 (002), 27.08 (101), 34.37 (102), 42.15 (110), 45.87 (103), 49.59 (112)).

TEM images of CdSe and core/shell CdSe/$Zn_{1-x}Mn_xS$ are shown in Figure 2A and B. The images reveal uniform and monodispersed particles with an average size of 4.1 and 4.7 nm for the CdSe and core/shell CdSe/$Zn_{1-x}Mn_xS$ nanoparticles, respectively. The increase in particle size is consistent with the formation of core/shell structure.

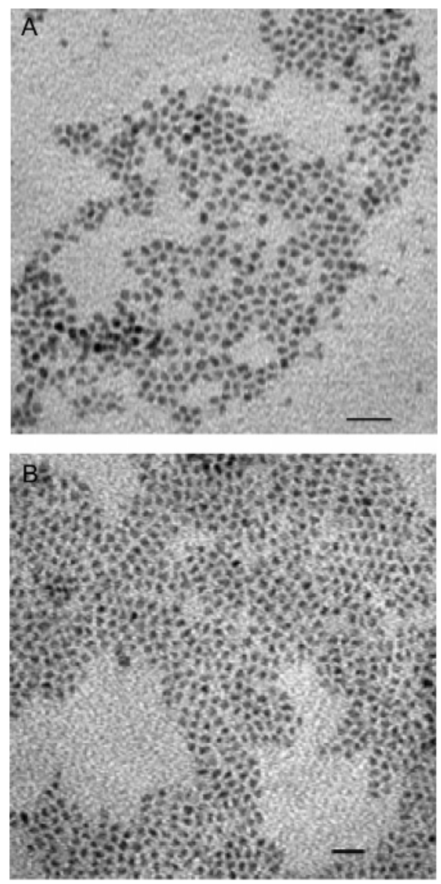

Figure 2. TEM micrographs of nanoparticles from a typical synthesis showing diameters of (A) 4.1 nm for CdSe nanoparticles, and (B) 4.7 nm for the coated core/shell CdSe/$Zn_{1-x}Mn_xS$ nanoparticles prepared via Scheme 1. Scale bar = 20 nm.

EPR measurements confirm that manganese is incorporated into the shell. The EPR spectra for samples of increasing Mn^{2+} doping levels are given in Figure 3. The samples for EPR measurement were purified via the solvent pair of chloroform/methanol four times followed by ligand exchange with pyridine to fully remove unreacted or free Mn^{2+} on the surface of particles.[20,31] The spectra are characterized by a six-line pattern superposed on a broad background line. The g value is in the

(34) Xie, R.; Kolb, U.; Li, J.; Basche, T.; Mews, A. *J. Am. Chem. Soc.* **2005**, *127*, 7480−7488.

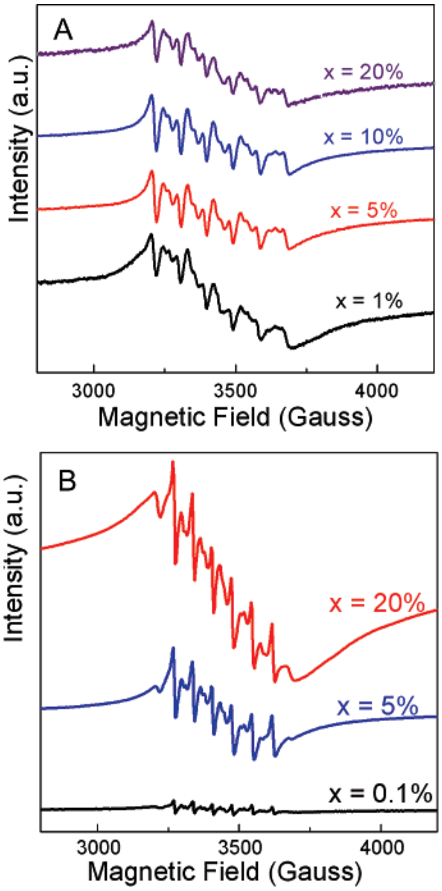

Figure 3. EPR spectra of CdSe/$Zn_{1-x}Mn_xS$ nanoparticles with different thicknesses of the shell: (A) approximately 1.5, and (B) 6 monolayers (x based on the initial amount of Mn^{2+} precursor).

range of 2.014−2.017, decreasing with increasing Mn^{2+} concentration, and this parameter is consistent with that of Mn^{2+} in hexagonal ZnS.[35] The average $|A_{Mn}|$ value is dependent on the thickness of the shell. For the nanoparticles with ∼1.5 monolayer shell, the hyperfine splitting is close to 90 G (Figure 3A). This value is similar to the hyperfine splittings observed for Mn^{2+} isolated on the surface of CdSe[20] rather than in the bulk,[22] consistent with a thin shell that effectively localizes Mn^{2+} ions near or at the surface rather than in the interior. We can attribute the six-line pattern and broad background line to Mn^{2+} in a crystallographically distorted matrix of ZnS due to the very thin shell (less than 0.5 nm).[36] To further investigate Mn^{2+} localization, nanoparticles with thicker shells were prepared. For nanoparticles with ∼6 monolayer shell, the hyperfine splitting is close to 69 G, which is consistent with observations reported for Mn^{2+} in a 2−3 nm ZnS matrix (Figure 3B).[37] The decreasing hyperfine splitting indicates that the thicker shell provides a more ordered matrix for Mn^{2+}. The EPR spectra were obtained after purification and pyridine extractions of the nanoparticles and are consistent with Mn^{2+} ions incorporated into the ZnS shell rather than simply physisorbed onto the surface. The EPR spectra show hyperfine splitting at all levels of Mn^{2+} doping in CdSe/$Zn_{1-x}Mn_xS$ samples; this is in contrast to broad EPR resonances without splitting reported for $Zn_{1-x}Mn_xS$ particles.[38] Broadening and loss of hyperfine splitting in $Zn_{1-x}Mn_xS$ particles have been attributed to the formation of manganese clusters. Our EPR results are more consistent with Mn^{2+} homogeneously distributed in $Zn_{1-x}Mn_xS$ shells, in which the ZnS shell is not a highly ordered structure and Mn^{2+} can facilely substitute for Zn^{2+}.

Table 1. Determination of Mn^{2+} Content for Core/Shell CdSe/$Zn_{1-x}Mn_xS$ Nanoparticles from AA Analysis and Corresponding Relaxivity Parameters from MRI Measurements

	AA results			relaxivity
initial amount, x%	after chloroform isolation, %	after pyridine exchange, %	Mn^{2+} ions per particle	r_1 (mM^{-1} s^{-1})
1	0.7	0.6	2	13.1
5	3.7	3.3	15	10.7
10	5.6	5.1	21	12.1
20	7.4	6.2	29	15.0
5[a]	0.87	0.87	28	13.8
20[a]	1.8	1.7	52	18.0

[a] Samples capped with ∼6 monolayers $Zn_{1-x}Mn_xS$ shell; all others were capped with ∼1.5 monolayer shell.

The amount of manganese incorporated in the shell was measured in all samples by atomic absorption as summarized in Table 1. Manganese content for the nanoparticle preparation was assessed after washing with the solvent pair of chloroform/methanol four times, and also after two additional pyridine exchanges[31] to determine if any metal was surface bound. Excess Mn^{2+} binds with TOPO or TOP and is removed during the wash process. The results show that a higher fraction of the initial manganese was incorporated into the shell when the synthesis was performed at a higher ratio of Mn^{2+} to Zn^{2+}. Little to no change in manganese quantity was found after the pyridine washes, indicating that in most cases little free manganese is found on the surface after chloroform isolation. For the thicker shell (∼6 monolayers) capped particles, the ratio of Mn^{2+} to Zn^{2+} incorporated was much lower than in the thinner shell (∼1.5 monolayer), although they were synthesized with the same initial concentration of manganese. This is consistent with the Mn^{2+} in the thin shell occupying a distorted local structure due to the lattice mismatch between the CdSe core and $Zn_{1-x}Mn_xS$ shell. Materials with this structure have much higher Gibbs free energy and entropy in comparison with well-ordered crystalline structures and, therefore, accept impurities more easily. It is more difficult to incorporate Mn^{2+} into the ordered layers of the thicker shell. The Mn^{2+} determined by AA for these quantum dots is proposed to be chemically bonded instead of physically absorbed on the surface, because it cannot be removed by multiple steps of chloroform/methanol washing followed by pyridine exchange. To confirm this, a control experiment was performed by heating the CdSe core and dimethylmanganese agent with the same experimental conditions for the shell growth but without the use of zinc and sulfur precursors. After purification, no manganese was detected by AA analysis, indicating that Mn^{2+} cannot be bound to the surface without the existence of ZnS matrix. The number of Mn^{2+} ions incorporated into each particle was evaluated on the basis of the concentration of Cd^{2+} and Mn^{2+} from AA results and the core size estimated from the function of the band gap energy

(35) Yeom, T. H.; Lee, Y. H.; Hahn, T. S.; Oh, M. H.; Choh, S. H. *J. Appl. Phys.* **1996**, *79*, 1004−1007.
(36) Borse, P. H.; Srinivas, D.; Shinde, R. F.; Date, S. K.; Vogel, W.; Kulkarni, S. K. *Phys. Rev. B: Condens. Matter* **1999**, *60*, 8659−8664.
(37) Igarashi, T.; Isobe, T.; Senna, M. *Phys. Rev. B: Condens. Matter* **1997**, *56*, 6444−6445.
(38) Gonzalez Beermann, P. A.; McGarvey, B. R.; Muralidharan, S.; Sung, R. C. W. *Chem. Mater.* **2004**, *16*, 915−918.

versus the particle sizes.[32] The band gap energy was determined by the absorbance spectra of the CdSe core.[39] As shown in Table 1, from the same initial amount of manganese precursor, more Mn^{2+} was incorporated into nanoparticles capped with the thicker shells.

Optical properties of the nanoparticles (thin shells), shown in Figure 4, indicate that shell formation was successful and that the addition of the manganese to the ZnS shell did not quench luminescence. Figure 4A presents the absorbance and luminescence spectra of CdSe nanoparticles of different diameters (absorbance, black; emission, red; from top to bottom: 8.0, 4.6, 3.8, 3.5 nm) and the corresponding core/shell CdSe/$Zn_{1-x}Mn_xS$ nanoparticles (x = 5%, where x = the initial amount of Mn^{2+} precursor as in Scheme 1; absorbance, purple; emission, blue). The overall shape of the absorbance spectra was maintained after the shell coating. However, the band edge shows a slight red shift, and the absorbance intensity decreased after the growth of the shell. The red shift has been explained by the formation of a relatively narrower band gap in core/shell CdSe/$Zn_{1-x}Mn_xS$ than that in CdSe nanoparticles due to the perturbation of the wider band gap shell of $Zn_{1-x}Mn_xS$.[40] The decrease of the band gap in core/shell CdSe/$Zn_{1-x}Mn_xS$ as compared to CdSe nanoparticles is expected to reduce the absorption intensity because the molar absorption coefficient of light (α) depends on the photon energy (E_g) near threshold, and the relationship between them can be expressed as:[41]

$$\alpha(h\nu) \propto (E_g - h\nu)^{1/2}$$

Luminescence spectra in Figure 4A are also red-shifted after the capping of the shell. In addition, the intensity of luminescence increased around 2−3 times for all of the Mn^{2+}-doped samples. Because of the size of the CdSe cores, the emission spectra are centered at different wavelengths ranging from ~570 to 650 nm, and an increase in luminescence after capping is observed for all sizes surveyed. This result confirms that the fluorescence emission is not simply due to contributions from Mn^{2+} in $Zn_{1-x}Mn_xS$ shell; Mn^{2+} with T_d site symmetry has an emission peak typically centered at 580−590 nm due to its $^4T_1 \rightarrow {}^6A_1$ transition.[24] The lack of Mn^{2+} emission is consistent with the EPR results, suggesting that Mn^{2+} is not in a highly ordered ZnS shell structure. However, even with the thicker ZnS shell, no emission from tetrahedral Mn^{2+} can be discerned. This may either be due to the low intensity of the Mn^{2+} emission as compared to CdSe or because even in the thicker shell (~6 monolayers) Mn^{2+} is in a locally disordered structure, thus quenching any emission from a tetrahedral Mn^{2+} ion.

We also prepared a series of core/shell CdSe/$Zn_{1-x}Mn_xS$ doped with varying amounts of Mn^{2+} with the same size of CdSe core, to investigate the dependence of their optical properties on the doping level of Mn^{2+}. As shown in Figure 4B, the fluorescence intensity increases after capping the CdSe core (black) with $Zn_{1-x}Mn_xS$ shells of varying Mn^{2+} amounts. The intensity of the emission decreases with increasing Mn^{2+} doping up to x = 10% (x = stoichiometric amount of reagent, actual Mn^{2+} incorporated = ~5%) but still remains higher than uncapped ones; however, larger amounts (x = 20%, actual Mn^{2+} = ~6%) decrease the intensity as compared to the uncapped CdSe core. In addition to the surface capping, fluorescence efficiency also depends on the quality of the CdSe core. As prepared, the quantum yields (QY) of the CdSe/$Zn_{1-x}Mn_xS$ nanoparticles were typically in the range of 30−60%. The shell thickness was controlled as ~1.5 monolayers for all of the

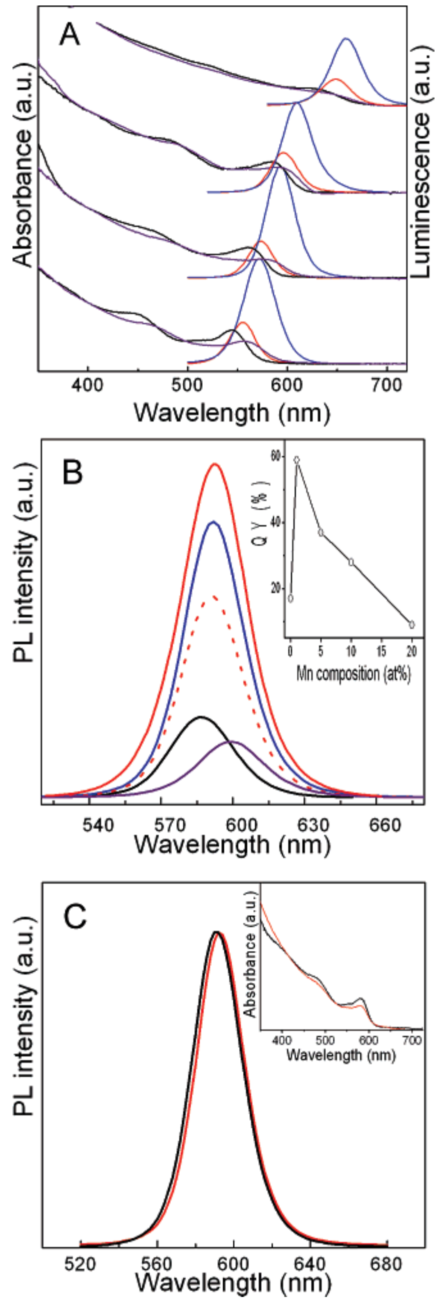

Figure 4. Core optical properties are maintained after capping and manganese doping. (A) Absorption and photoluminescence (PL) emission spectra for CdSe and CdSe/$Zn_{1-x}Mn_xS$ (x = 5%) with different core sizes. From top to bottom, nanoparticle sizes were = 8.0, 4.6, 3.8, and 3.5 nm: CdSe (absorbance = black, emission = red), core/shell CdSe/$Zn_{1-x}Mn_xS$ core/shell (absorbance = purple, emission = blue); (B) PL spectra of CdSe (black) and CdSe/$Zn_{1-x}Mn_xS$ with varying doping amounts (based on the intial amount of Mn^{2+} precursor) of Mn^{2+} (x), 1% (red), 5% (blue), 10% (dotted red), 20% (purple). Inset: Quantum yield (QY) of CdSe and CdSe/$Zn_{1-x}Mn_xS$ versus initial doping amount. (B) Normalized PL emission spectra of CdSe/$Zn_{0.9}Mn_{0.1}S$ in chloroform (black) and in water (red). Inset: Corresponding absorbance spectra in chloroform (black) and in water (red).

(39) Wang, Y.; Suna, A.; Mahler, W.; Kasowski, R. *J. Chem. Phys.* **1987**, *87*, 7315−22.
(40) Peng, X. G.; Schlamp, M. C.; Kadavanich, A. V.; Alivisatos, A. P. *J. Am. Chem. Soc.* **1997**, *119*, 7019−7029.
(41) Trindade, T.; O'Brien, P.; Pickett, N. L. *Chem. Mater.* **2001**, *13*, 3843−3858.

samples in the study because the shell thickness in the range of 1−2 monolayers typically provides the maximum quantum efficiency.[26,40] The decrease in photoluminescence efficiency in the samples at higher Mn^{2+} doping levels may be due to the presence of interfacial Mn^{2+} between the core of CdSe and the ZnS shell.[23] The desired sites for incorporation of Mn^{2+} are within the shell and not at the surface of the CdSe core. However, at high Mn^{2+} concentration, Mn^{2+} may be present at the interface between the core and the shell. Surface Mn^{2+} has been observed to influence the optical emission property of ZnS[42] and may also affect that of CdSe in the present samples. The emission of core/shell CdSe/$Zn_{1-x}Mn_xS$ is related to the electronic structure of the shell,[43] which is affected by the presence and the doping amount of Mn^{2+}.[42] It is well-known that the growth of a semiconductor shell with higher band gap around the core can improve the quantum efficiency due to the reduced effect of surface defects[44] and due to quantum confinement.[40,45] The lattice mismatch between ZnS and CdSe is 12%, and it may decrease with the doping of Mn^{2+} into the ZnS shell because Mn^{2+} is about 10% in diameter bigger than Zn^{2+}. Doping with more Mn^{2+}, however, may increase the amount of interfacial Mn^{2+}, providing a site for nonradiative recombination of the electron−hole pair in the CdSe core. It may be possible, by means of sequentially adding a ZnS and then a $Zn_{1-x}Mn_xS$ layer, to prevent the reduction in QY, and further studies are underway.

The core/shell nanoparticles were rendered water-soluble by coating with octylamine-modified poly(acrylic) acid (average molecular weight: 8000) as illustrated in Scheme 1. The percentage of carboxyl groups in the polymer that are modified with octylamine molecules affects the solubility and the luminescence efficiency of the nanoparticles in water. We found that modifying ∼45% of carboxyl groups resulted in optimal physical properties. Above this value, the capping resulted in bright, water-insoluble (or partially soluble) particles, whereas below this value it resulted in very soluble, but less bright particles. Figure 4C shows the normalized absorbance (inset) and fluorescence of the nanoparticles before coating (black, in chloroform) and after coating (red, in water). The emission spectra are almost identical for the nanoparticles in the two different media. Luminescence efficiency, however, decreased in water. Quantum yield for the QDs, thick or thin shell, ranged from 7% to 21% in water. The reduction of QY during the transfer from organic phase to water results from a combination of different effects. First, isolation of the nanoparticles decreased the QY by ∼10−20% due to the loss of TOPO and HDA molecules on the surface of the nanoparticle. The further decrease of QY in water can be attributed to a dipole effect: the access of the water molecules to the QDs surface and the interaction of the polymer molecules with the QDs surface. These QY values in water are comparable to those reported in the literature for silanization,[46] and other water-soluble coatings, for example, peptide coating.[47] We found that quantum yield was dependent on the quality of the QDs and the polymer coating process. Further optimization of the polymer coating technique to preserve high QY is ongoing. After being coated with the polymer, the nanoparticles were suspended in water, and their magnetic properties were determined by magnetic resonance imaging on a 7 T instrument.

The MRI signal arises from perturbation of the magnetic moments of proton (^{1}H) nuclei from water when placed in a strong magnetic field. Typical clinical contrast mechanisms are based on tissue-specific differences in the proton density and transverse or longitudinal proton relaxation times, T_2 or T_1, respectively. Where tissue differences in relaxation times do not occur, an exogenous, paramagnetic agent may be applied to enhance contrast. Typical paramagnetic agents act to decrease proton relaxation times, specifically T_1 relaxation times. Relaxivity (r_1), a concentration-independent measure of the effectiveness of a paramagnetic material, is derived from the slope of inverse relaxation time versus concentration. Relaxivities for the CdSe/$Zn_{1-x}Mn_xS$ nanoparticles are shown in Table 1. The r_1 values (10−18 $mM^{-1}\ s^{-1}$) are much greater than those observed for typical manganese agents at much lower field strength (MnDPDP (DPDP = *N*,*N*′-dipyridoxylethylenediamine-*N*,*N*′-diacetate-5,5′- bis(phosphate)) = 1.6 $mM^{-1}\ s^{-1}$, $MnCl_2$ = 6.9 $mM^{-1}\ s^{-1}$, both at 0.47 T).[48,49] The r_1 for manganese agents is known to decrease with increasing field strength (e.g., optimal r_1 at ∼0.47 T for certain Mn(II) EDTA complexes[48]); therefore, we anticipate that the r_1 at lower, clinical field strengths will be higher than those measured at 7 T reported here. We attribute the increased r_1 for the multifunctional quantum dots, as compared to manganese chelates, to a combination of slower rotation and high localized Mn^{2+} concentration. It is well-known that relaxivity of low molecular weight species such as manganese chelates can be increased by slowing their rotation, commonly achieved by coupling the paramagnetic ions to large molecular weight species.[50] Localization of the Mn^{2+} ion in the nanoparticles slows rotation; confinement to the shell is also predicted to slow rotation. Relaxivities for the thick shell nanoparticles were comparable to their thin shell equivalents, with greater r_1 relaxivity for higher total Mn^{2+} content as expected.

The utility of the water-soluble nanoparticles as dual-mode imaging agents was investigated in solution and on cells in culture. Nanoparticles in solution were observed by magnetic resonance imaging, digital photography, and confocal microscopy to confirm that manganese content was sufficient to produce contrast in an MR image at reasonable concentrations and that quantum yield was sufficient to produce optical contrast at these concentrations. Particles were dissolved in water at concentrations of 0.024, 0.049, 0.097, and 0.194 mM Mn^{2+} with water as a blank. Relaxation time T_1 was measured at 7 T and 21 °C using a saturation recovery sequence. T_1-weighted images are shown in Figure 5A. With T_1 weighting, increasing manganese concentration produces higher signal intensity as

(42) Sooklal, K.; Cullum, B. S.; Angel, S. M.; Murphy, C. J. *J. Phys. Chem. B* **1996**, *100*, 4551−4555.
(43) Zhang, F. C.; Luo, H.; Dai, N.; Samarth, N.; Dobrowolska, M.; Furdyna, J. K. *Phys. Rev. B: Condens. Matter* **1993**, *47*, 3806−10.
(44) Nirmal, M.; Dabbousi, B. O.; Bawendi, M. G.; Macklin, J. J.; Trautman, J. K.; Harris, T. D.; Brus, L. E. *Nature* **1996**, *383*, 802−804.
(45) Haus, J. W.; Zhou, H. S.; Honma, I.; Komiyama, H. *Phys. Rev. B: Condens. Matter* **1993**, *47*, 1359−65.
(46) Gerion, D.; Pinaud, F.; Williams, S. C.; Parak, W. J.; Zanchet, D.; Weiss, S.; Alivisatos, A. P. *J. Phys. Chem. B* **2001**, *105*, 8861−8871.
(47) Doose, S.; Tsay, J. M.; Pinaud, F.; Weiss, S. *Anal. Chem.* **2005**, *77*, 2235−2242.
(48) Troughton, J. S.; Greenfield, M. T.; Greenwood, J. M.; Dumas, S.; Wiethoff, A. J.; Wang, J.; Spiller, M.; McMurry, T. J.; Caravan, P. *Inorg. Chem.* **2004**, *43*, 6313−6323.
(49) Nordhoy, W.; Anthonsen, H. W.; Bruvold, M.; Brurok, H.; Skarra, S.; Krane, J.; Jynge, P. *Magn. Reson. Med.* **2004**, *52*, 506−514.
(50) Caravan, P.; Ellison, J. J.; McMurry, T. J.; Lauffer, R. B. *Chem. Rev.* **1999**, *99*, 2293−2352.

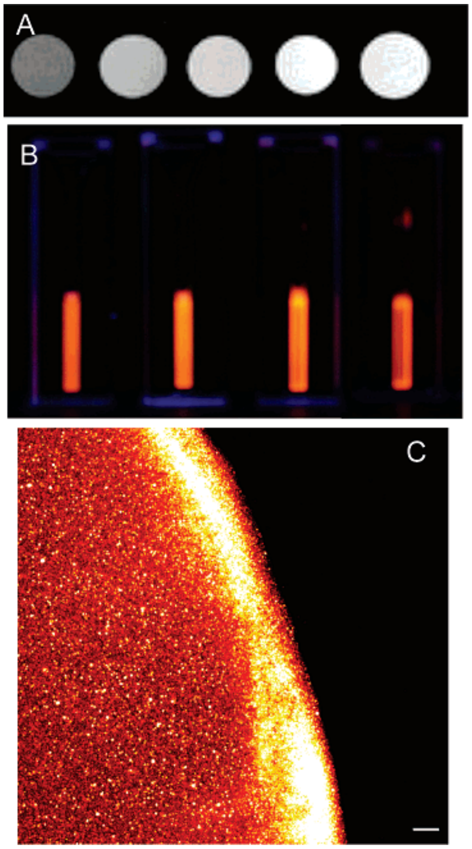

Figure 5. Multimodal core/shell quantum dots are detectable by MRI and optical methods. (A) MR detection. Nanoparticles imaged by T_1-weighted MRI show increasing signal intensity as Mn^{2+} concentration increases (from left to right, 0.0, 0.024, 0.049, 0.097, 0.194 mM Mn^{2+}). (B) Optical detection. By eye, nanoparticles at 0.024, 0.049, 0.097, 0.194 mM Mn^{2+} (left-right), illuminated by handheld UV lamp, show no decrease in emission intensity with dilution. (C) Image of droplet of nanoparticles from confocal microscopy. Nanoparticles at 100 μM Mn^{2+} concentrations give a strong signal in fluorescence image. Pooling of nanoparticles at the meniscus of the drop causes the halo effect observed.

expected (top row). To demonstrate that the concentrations of nanoparticles used for MR imaging are also brightly luminescent, samples of the same concentrations of nanoparticles employed for the MR studies were photographed using only a handheld UV lamp as excitation (Figure 5B). By eye, there is no detectable difference in intensity between concentrations, indicating that even the lowest concentration saturated the detector (eye). The high intensity of emission observed under these weak excitation conditions indicates the strength of the luminescence efficiency. As additional confirmation that the nanoparticles possess ample luminescence for optical imaging, solutions of nanoparticles were dropped on glass slides for imaging by scanning laser confocal microscopy. Nanoparticles at a concentration of ~100 μM Mn^{2+} in water, a concentration that produced high signal enhancement for MRI in the above experiments,[51] were dropped on a glass slide and imaged by confocal microscopy with 405 nm diode laser excitation, 560 nm long pass filter at detector. Saturation of the detectors was observed even at moderate laser power levels, again indicating very strong luminescence (Figure 5C).

As a preliminary investigation of the utility of the multimodal quantum dots for biological applications, the nanoparticles were applied to cells in culture. Macrophages were incubated with the nanoparticles at 0.408 mM Mn^{2+}, similar to one of the lowest concentrations used for the solution only measurements, for 1 h and then imaged by confocal microscopy with 488 nm diode excitation. Uptake of the nanoparticles is clearly visible as punctate spots of luminescence in the cytoplasm of the cells (Figure 6). This pattern of signal is consistent with an endocytic or phagocytic mode of internalization.[52] Three-dimensional confocal image volumes of the cells verify that the signal originates from the cytoplasm and not from aggregates on the cell surface. Confocal image slices through the cells in Figure 7 demonstrate that signal is present in the cell interior rather than on the surface. Luminescence signal appears as punctate spots in all slices, whereas surface staining would appear as peripheral rings in each slice. In addition, as the slices advance from the apical to basal surface of the cells (Figure 7A−I), signal appears primarily in the centermost slices. Note that the scan time per slice (details in materials and methods) was faster for the volume acquisition, accounting for the lower signal intensities observed in these images. The cells were then lysed and imaged by MRI as shown in Figure 8. In a T_1-weighted image, cells from the optical studies that were incubated with quantum dots (right) show significant contrast enhancement from unlabeled cells (left). These images demonstrate that the same range of applied concentration can produce contrast for both optical and MR imaging and illustrate the dual-mode utility of these nanoparticles for imaging. These preliminary studies on cells reflect internalization by nonspecific mechanisms. For future applications, targeting moieties can be conjugated to the surface of the nanoparticles to direct uptake by specific molecules under investigation.

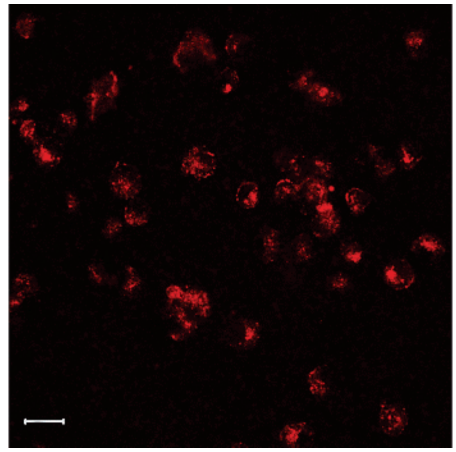

Figure 6. Cells internalize sufficient multimodal quantum dots for detection by confocal microscopy. Macrophages incubated with the nanoparticles show a pattern of punctate staining characteristic of endocytic uptake. Scale bar = 20 μm.

Conclusions

In conclusion, we have synthesized a series of paramagnetic and luminescent nanoparticles with high quantum yield and relaxivity for use in combined optical and MRI techniques. The methodology described here allows incorporation of high levels of paramagnetic material into quantum dots without sacrificing luminescence quantum yield, which represents a significant

(51) Ahrens, E.; Rothbacher, U.; Jacobs, R.; Fraser, S. *Proc. Natl. Acad. Sci. U.S.A.* **1998**, *95*, 8443−8448.

(52) Koval, M.; Preiter, K.; Adles, C.; Stahl, P. D.; Steinberg, T. H. *Exp. Cell Res.* **1998**, *242*, 265−273.

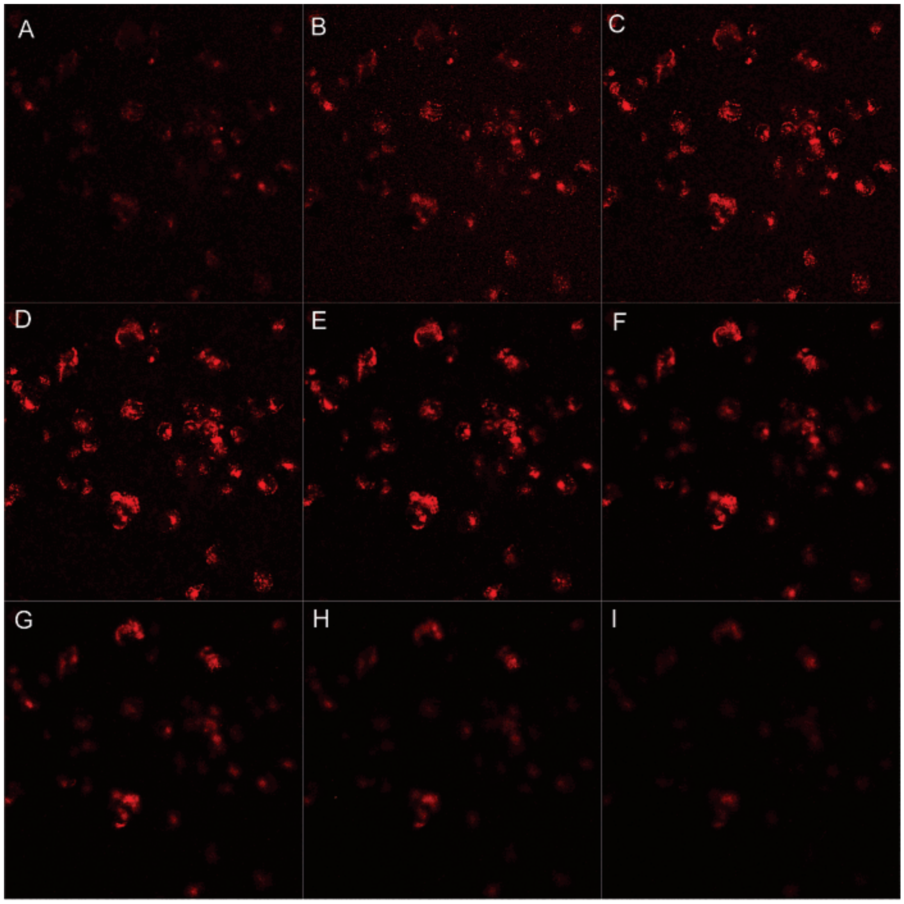

Figure 7. Quantum dots are internalized. Confocal slices through a volume of cells incubated with the multimodal quantum dots show that the signal originates from the cell interior and not from material adhered to the surface. Image slices advance through the cell volumes starting at the apical surface and moving basally from A to I.

Figure 8. Internalized quantum dots produce MRI contrast. T_1-weighted images from tubes containing cell lysates show that lysates of cells that have been incubated with quantum dots (right) show significant contrast enhancement as compared to cells that have not been exposed to quantum dots. These samples were from cells in the same experiment shown for the optical uptake studies of Figures 6 and 7. Images are 0.5 cm in diameter.

breakthrough in the development of multimodal imaging probes based on quantum dots. The layered quantum dot design avoids the use of environmentally sensitive organic dyes and capitalizes on the exquisite stability of quantum dot emission to degradation, environment, or bleaching. The amount of magnetic dopant can also be easily modified. Applications include using these nanoparticles to label specific molecular events in disease. In addition to the cancer application mentioned in the introduction, another application would be to target the multimodal nanoparticles to atherosclerotic plaques. MRI could be used to identify and image the plaques in vivo, and then the optical emission would be used to guide endoscopic interventions at those locations identified by MRI to contain plaques. The method presented is a general synthetic method that can also be applied to quantum dots that emit in the near-IR. Such multimodal methods hold great promise for improving diagnosis and therapy of diseased states.

Acknowledgment. We thank Drs. Gregory J. Yeagle and R. David Britt for assistance with the EPR measurements, Sungjin Cho and John Neil for assistance with XRD, and Hsiang Wei Chiu for assistance with TEM. This work was supported by awards from the NSF (NIRT-0210807, NER-0508527), NIH (EB000993-01A1), Whitaker Foundation (RG-02-0740), and the UC Davis NMR facility.

JA065996D